

Multiple-Scattering Microfacet BSDFs with the Smith Model

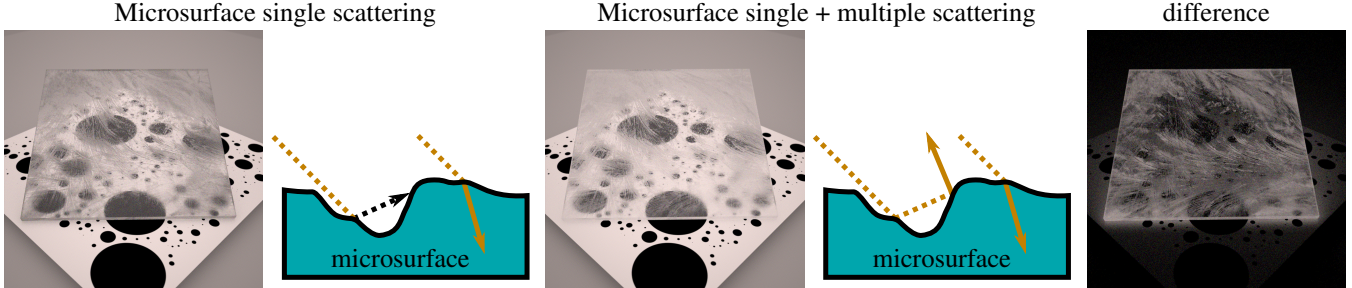
Eric Heitz¹Johannes Hanika¹Eugene d'Eon²Carsten Dachsbaecher¹¹Karlsruhe Institute of Technology²8i

Figure 1: A dielectric plate with textured GGX roughness ($\alpha = 0 \dots 1, \eta = 1.5$). (Left) Traditional BSDFs consider only single scattering on microsurfaces, thereby neglecting significant energy where roughness is high. (Middle) Our new BSDF includes all orders of multiple scattering on microsurfaces and achieves 100% energy conservation with only 19% more render time in this scene. (Right) Visualization of the energy in the middle image that arises from paths that have at least one multi-microsurface interaction.

Abstract

Modeling multiple scattering in microfacet theory is considered an important open problem because a non-negligible portion of the energy leaving rough surfaces is due to paths that bounce multiple times. In this paper we derive the missing multiple-scattering components of the popular family of BSDFs based on the Smith microfacet model. Our derivations are based solely on the original assumptions of the Smith model. We validate our BSDFs using raytracing simulations of explicit random Beckmann surfaces.

Our main insight is that the microfacet theory for surfaces with the Smith model can be derived as a special case of the microflake theory for volumes, with additional constraints to enforce the presence of a sharp interface, i.e. to transform the volume into a surface. We derive new free-path distributions and phase functions such that plane-parallel scattering from a microvolume with these distributions exactly produces the BSDF based on the Smith microfacet model, but with the addition of higher-order scattering.

With this new formulation, we derive multiple-scattering microfacet BSDFs made of either diffuse, conductive, or dielectric material. Our resulting BSDFs are reciprocal, energy conserving, and support popular anisotropic parametric normal distribution functions such as Beckmann and GGX. While we do not provide closed-form expressions for the BSDFs, they are mathematically well-defined and can be evaluated at arbitrary precision. We show how to practically use them with Monte Carlo physically based rendering algorithms by providing analytic importance sampling and unbiased stochastic evaluation. Our implementation is analytic and does not use per-BSDF precomputed data, which makes our BSDFs usable with textured albedos, roughness, and anisotropy.

CR Categories: I.3.7 [Computer Graphics]: Three-Dimensional Graphics and Realism—Ray tracing;

Keywords: Microfacet theory, BRDF, BSDF, multiple scattering, anisotropic media

1 Introduction

The rendering of photorealistic images is based on two main pillars: a global illumination method for computing light transport in a scene, and reflection or scattering models to reproduce the appearance of real materials. This paper advances in the latter field, where microfacet theory constitutes a powerful and widely used means to describe the interaction of light with rough surfaces.

The concept of modeling rough surfaces with randomly oriented microfacets was developed in the 1960s [Beckmann and Spizzichino 1963]. Microfacet light reflectance theory began shortly thereafter in physics [Smith 1967; Torrance and Sparrow 1967] with practical single-scattering microsurface reflectance models first introduced to graphics by Cook and Torrance [1982] and later generalized [Stam 2001] to consider both reflection and transmission, forming the combined *bidiirectional scattering distribution function* (BSDF). This microfacet framework is quite general, permitting a variety of facet distributions such as Beckmann and GGX [Walter et al. 2007]. Nearly all parametric BSDFs in rendering today use or have been inspired by microfacet theory [Hill et al. 2015].

Despite the prevalence of microfacet theory—especially in physically based rendering—nearly all popular parametric BSDFs consider only single scattering from the microsurface, i.e. they account for self-shadowing and masking of reflected/refracted light, but omit the outgoing light that would scatter multiple times between microfacets (Fig. 1). However, accurately accounting for microsurface multiple scattering events is required to ensure energy conservation and to exhibit important aspects of appearance, such as strong color saturation in highlights on rough conductors, or to accurately predict transmission through dielectric plates (Fig. 1). Thus, modeling multiple scattering is considered an important unsolved problem in microfacet theory.

In this paper, we show how to model multiple scattering with the Smith microsurface model. Our key insight is that—subject to its assumptions—scattering from surface microfacets can be formulated as a volumetric scattering process using a new variant of microflake theory [Jakob et al. 2010]. Given a microfacet distribution (Beckmann, GGX) and a material property (conductor, dielectric, diffuse) we derive free-path distributions and phase functions for

a new variety of volumes. Further, because the microfacets are not uniformly oriented in the volumes, the phase function is of the anisotropic-media (microflake) kind. By generalizing volumetric scattering in this way, we produce a *microvolume* whose plane-parallel reflectance is identical to the reflectance from the original *microsurface* model. However, in contrast to the surface-based approach, the volumetric scattering framework enables us to find practical ways to model multiple scattering.

In practice, we express surface scattering as the plane-parallel scattering from a microvolume, computed efficiently using a low-variance Monte Carlo estimator (a random walk). The distribution arising from the single-scattering component of this random walk has an analytic expression: it exactly produces the single-scattering Smith BSDFs [Walter et al. 2007]. For surfaces with plausible roughness, the random walks are very short and can be included directly inside of Monte Carlo rendering algorithms. Note that our volume-scattering process models the interaction with a surface, but its application in rendering is virtual in that no displacements occur, i.e. the incident and exitant location are the same and the resulting plane-parallel radiometry produces a BSDF.

Our derivations are general and support a variety of anisotropic microfacet distributions. Our volume scattering model relies only on the original physical assumptions of the Smith model. For further physical validation we compare the single and multiple scattering predicted by our model to Monte Carlo simulations of explicit random anisotropic Beckmann surfaces.

In summary, our paper makes the following contributions:

- Deriving the free-path distributions for volumetric media that correspond to the Smith microsurface (Sec. 5).
- Deriving the phase function for the volumetric-scattering interpretation of the Smith microsurface (Sec. 6).
- Introducing a random-walk approach to microsurface scattering based on the volumetric free paths and phase functions (Sec. 7).
- Defining the multiple-scattering BSDF of the Smith model based on the statistical expectation of the random walks (Sec. 8).
- Explaining how to implement the multiple-scattering BSDF as a classic material plugin in a rendering engine with importance sampling, stochastic evaluation, and optimizations that reduce the variance of the stochastic estimate.

2 Previous Work

There is an enormous body of work on reflectance from rough surfaces. Our focus here is limited to parametric BSDFs.

Microsurface Multiple Scattering in Graphics Very few works in graphics consider microsurface multiple scattering.

The BRDF proposed by Kelemen et al. [2001] could be considered the first to move beyond the non-physical linear combination of specular and Lambertian lobes by proposing a specular-albedo-modulated diffuse term derived with reciprocity and energy conservation in mind. By design, this BRDF enforces an azimuthally invariant multiple-scattering lobe, which our ground-truth simulation shows to be inaccurate. Further, anisotropic materials and transmission were not treated. Jakob et al. [2014] introduced a general framework for multilayer materials with rough interfaces, including scattering between layers. In this work, they generalize (in the Fourier domain) the heuristic of Kelemen et al. to transmission.

This approach reintroduces much of the missing energy of previous BSDF models, but inherits the unphysical azimuthal invariance of the multiple scattering. Furthermore it requires an involved implementation with precomputed tables of Fourier coefficients and has limited application for textured materials. The fundamental difference with our work is that these BRDFs are not associated with microsurface *models*, i.e. they do not make *predictions* regarding the light transport emerging from a microsurface defined by specific assumptions. Hence, they can be regarded as *techniques* used to enforce energy conservation in BSDFs. In contrast, we are interested in deriving the multiple scattering *predicted* by the assumptions of the Smith microsurface *model*; energy conservation comes naturally as a side effect of the model.

For the case of V-groove microsurfaces with Lambertian properties, a double-scattering model was proposed by Oren and Nayar [1995]. In the specific case of spherically shaped surface dents, interreflections for either mirror or diffuse properties have analytic solutions [Koenderink et al. 1999]. In this paper, we investigate the Smith model, which is known to be the most physically realistic geometric-optics model and regarded as the state of the art in computer graphics [Hill et al. 2015].

Microsurface Multiple Scattering in Physics Several works in physics [Bourlier and Berginc 2004; Li et al. 2011; Li et al. 2013; Li et al. 2014] focus on the albedo of rough surfaces with consideration of multiple scattering, but do not derive a full BSDF. To the best of our knowledge, we are the first in either graphics or physics to derive and validate the complete radiometry of Smith microsurface scattering. In physics, microfacet models are often validated against numerical simulations on explicit surfaces (e.g. noise functions). We apply the same validation methodology to our model.

Relation to Volumetric Scattering Our novel variant of participating media is related to several previous works. The scattering phase functions of our volume-scattering model involve a generalization of sampling from the *distribution of visible normals* and thus our phase function sampling builds on Heitz and d’Eon [2014]. Because the phase function depends on the incident direction, our volume-scattering model is typically referred to as *anisotropic media* [Kuščer and Summerfield 1969; Williams 1978] and described in graphics by *microflake theory* [Jakob et al. 2010; Heitz et al. 2015]. Plane-parallel reflectance from anisotropic media has been well studied in physics, particularly for the purpose of describing light transport in tree canopies [Furfaro and Ganapol 2007]. Our use of infinite densities to model a surface, together with methods for treating transmission for dielectrics, are (to the best of our knowledge) new.

3 Review of Microfacet Theory

In this section, we introduce the notations that will be used throughout this paper. For an exhaustive review of microfacet theory we refer the reader to [Heitz 2014].

Ω	spherical domain (4π steradians)
(θ, ϕ)	spherical coordinates:
ω	$\omega = (\cos \phi \sin \theta, \sin \phi \sin \theta, \cos \theta)$
$\omega_1 \cdot \omega_2$	dot product
$ \omega_1 \cdot \omega_2 $	absolute value of the dot product
$\langle \omega_1, \omega_2 \rangle$	dot product clamped to 0
$\chi^+(a)$	Heaviside function: 1 if $a > 0$ and 0 if $a \leq 0$
\mathcal{U}	uniform random number in $[0, 1]$

Table 1: Mathematical notation used in this paper.

$\omega_g = (0, 0, 1)$	geometric normal
$\omega_m = (x_m, y_m, z_m)$	microfacet normal
$\omega_i = (x_i, y_i, z_i)$	incident direction ($\omega_i \cdot \omega_g > 0$)
$\omega_o = (x_o, y_o, z_o)$	outgoing direction
τ	microsurface abscissa in (x, y) -plane
h	microsurface height on z -axis
$P^1(h)$	distribution of heights
$C^1(h)$	cumulative distribution of heights
$C^{-1}(U)$	inverse of C^1
$D(\omega_m)$	distribution of normals (NDF)
$D_{\omega_i}(\omega_m)$	distribution of visible normals (VNDF)
$\Lambda(\omega)$	the Smith Lambda function
$G_1(\omega_i, \omega_m)$	masking (height-averaged)
$G_1^{\text{local}}(\omega_i, \omega_m)$	masking (local)
$G_1^{\text{dist}}(\omega_i)$	masking (distant & height-averaged)
$G_1^{\text{dist}}(\omega_i, h)$	masking (distant) at height h
$G_1^{\text{dist}}(\omega_i, h, \tau)$	masking (at distance in $[0, \tau]$) at height h
$G_2(\omega_i, \omega_o, \omega_m)$	masking-shadowing
$f_m(\omega_i, \omega_o, \omega_m)$	material micro-BSDF
$f(\omega_i, \omega_o)$	rough material BSDF
$p(\omega_i, \omega_o)$	rough material phase function

Table 2: Physical quantities used in microfacet models.

3.1 The Smith Model

A statistical model of a random microsurface is described by its distributions of heights $P^1(h)$ and normals $D(\omega_m)$, where h is the displacement of the surface at some position measured from the average plane of the surface at $h = 0$. The main assumption of the Smith model [Smith 1967] is that these distributions are independent (heights and normals are uncorrelated) as illustrated in Fig. 2 and can thus be chosen independently. In order to satisfy the assumptions of the Smith model, it turns out that the final reflectances are independent of the particular choice of height distribution. For instance, using either the uniform or the Gaussian height distribution results in the same BSDF.

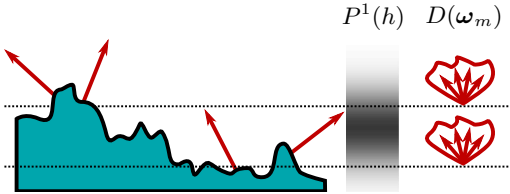


Figure 2: The Smith microsurface model. The normals of the microsurface are independent of their heights.

The Distribution of Heights The elevations h of a microsurface are distributed according to the *distribution of heights* $P^1(h)$. It is a *probability density function* (PDF) and we denote the *cumulative distribution function* (CDF) of heights as $C^1(h)$ and the inverse CDF as C^{-1} . In our supplemental material, we implement our model with the uniform and Gaussian distributions of heights.

The Distribution of Normals The distribution of normals $D(\omega_m)$ —commonly referred to as the *normal distribution function* (NDF)—describes the statistical distribution of the microfacets’ orientations. In our supplemental material, we implement our model with the anisotropic Beckmann and GGX distributions.

The Smith Masking Function A corollary of the Smith assumption is that the visibility of a *non-backfacing* point on the microsurface depends only on its height h and not on its normal ω_m . Hence,

the probability that a point is visible from a direction ω_i is the product of the local masking function $G_1^{\text{local}}(\omega_i, \omega_m) = \chi^+(\omega_i \cdot \omega_m)$ (omitting back-facing orientations) and the distant masking function

$$G_1^{\text{dist}}(\omega_i, h) = (C^1(h))^{\Lambda(\omega_i)}, \quad (1)$$

which is the probability that the ray does not intersect the microsurface. We provide more details on the function Λ in Section 5. The visibility of a point on the microsurface is then [Heitz 2014]:

$$G_1(\omega_i, \omega_m, h) = G_1^{\text{local}}(\omega_i, \omega_m) G_1^{\text{dist}}(\omega_i, h). \quad (2)$$

The distant masking function averaged over all heights is

$$G_1^{\text{dist}}(\omega_i) = \int_{-\infty}^{+\infty} G_1^{\text{dist}}(\omega_i, h) P^1(h) dh = \frac{1}{1 + \Lambda(\omega_i)} \quad (3)$$

and the masking function averaged over the heights is

$$G_1(\omega_i, \omega_m) = G_1^{\text{local}}(\omega_i, \omega_m) G_1^{\text{dist}}(\omega_i). \quad (4)$$

The Masking-Shadowing Function The masking-shadowing function is often obtained by neglecting correlations arising from the heights and using the product of two masking functions: $G_2(\omega_i, \omega_o, \omega_m) = G_1(\omega_i, \omega_m) G_1(\omega_o, \omega_m)$ [Walter et al. 2007]. However, considering the correlation of heights is necessary in order to model multiple scattering using a random walk on the microsurface. Thus we use the *height-correlated* distant masking-shadowing function [Heitz 2014]

$$G_2(\omega_i, \omega_o, \omega_m) = G_1^{\text{local}}(\omega_i, \omega_m) G_1^{\text{local}}(\omega_o, \omega_m) G_2^{\text{dist}}(\omega_i, \omega_o), \quad (5)$$

which is obtained by integrating the masking and shadowing functions over the heights

$$G_2^{\text{dist}}(\omega_i, \omega_o) = \int_{-\infty}^{+\infty} G_1^{\text{dist}}(\omega_i, h) G_1^{\text{dist}}(\omega_o, h) P^1(h) dh. \quad (6)$$

If ω_i and ω_o are on the same side of the microsurface (i.e. reflection), it has the closed form

$$G_2^{\text{dist}}(\omega_i, \omega_o) = \frac{1}{1 + \Lambda(\omega_i) + \Lambda(\omega_o)}. \quad (7)$$

If ω_i and ω_o are on opposite sides of the microsurface (transmission) it is [Pinel et al. 2005]

$$G_2^{\text{dist}}(\omega_i, \omega_o) = B(1 + \Lambda(\omega_i), 1 + \Lambda(\omega_o)), \quad (8)$$

where B is the Beta function. We provide a proof in Appendix A.

The Distribution of Visible Normals It is often useful to consider the distribution of normals visible to a uniform set of incoming rays along direction ω_i . In the Smith model with heights and normals being independent, the statistical distribution of normals ω_m visible from the incident direction ω_i does not depend on the height but only on the cosine factor of the normals:

$$D_{\omega_i}(\omega_m) = \frac{\langle \omega_i, \omega_m \rangle D(\omega_m)}{\int_{\Omega} \langle \omega_i, \omega_m \rangle D(\omega_m) d\omega_m}. \quad (9)$$

From this equation, we can see that the distribution is normalized, i.e. $\int_{\Omega} D_{\omega_i}(\omega_m) d\omega_m = 1$. An important property of the Smith model is that, because heights and normals are independent, the average distant masking function from Eq. (3) is also the normalization factor of the distribution of visible normals from Eq. (9):

$$D_{\omega_i}(\omega_m) = \frac{G_1^{\text{dist}}(\omega_i) \langle \omega_i, \omega_m \rangle D(\omega_m)}{\cos \theta_i} = \frac{\langle \omega_i, \omega_m \rangle D(\omega_m)}{\cos \theta_i (1 + \Lambda(\omega_i))}. \quad (10)$$

3.2 The Single-Scattering BSDF

In order to complete the overview of microfacet theory, we briefly recall the equations of the classic single-scattering BSDFs based on the Smith model.

Generic Rough Materials A single scattering rough BSDF f is obtained by integrating the product of the distribution of visible normals D_{ω_i} , the micro-BRDF f_m of the microfacets (i.e. the material of which the microsurface is made), and the probability that ω_m is visible for ω_o given that it is visible for ω_i (i.e. $\frac{G_2(\omega_i, \omega_o, \omega_m)}{G_1(\omega_i, \omega_m)}$):

$$f(\omega_i, \omega_o) = \frac{1}{\cos \theta_o} \quad (11)$$

$$\int_{\Omega} f_m(\omega_i, \omega_o, \omega_m) \langle \omega_o, \omega_m \rangle \frac{G_2(\omega_i, \omega_o, \omega_m)}{G_1(\omega_i, \omega_m)} D_{\omega_i}(\omega_m) d\omega_m.$$

Rough Dielectric If the material is dielectric, then the distribution of visible normals is transformed into a distribution of outgoing directions ω_o by *specular reflection* and *specular transmission*. The micro-BSDF of the material is [Walter et al. 2007]

$$f_m^{\text{dielectric}}(\omega_m, \omega_i, \omega_o) = \frac{F(\omega_i, \omega_{hr}) \delta_{\omega_{hr}}(\omega_m)}{4 |\omega_i \cdot \omega_{hr}|} + \frac{\eta_o^2 (1 - F(\omega_i, \omega_{ht})) \delta_{\omega_{hr}}(\omega_m)}{(\eta_i(\omega_i \cdot \omega_{ht}) + \eta_o(\omega_o \cdot \omega_{ht}))^2}, \quad (12)$$

where ω_{hr} and ω_{ht} are the half vectors of reflection and transmission, respectively, F is the Fresnel factor, and n_i and n_o are the indices of refraction of the incident and opposite sides, respectively. The rough dielectric BSDF is the sum of the BRDF $f_r^{\text{dielectric}}$ (reflection) and BTDF $f_t^{\text{dielectric}}$ (transmission):

$$f^{\text{dielectric}}(\omega_i, \omega_o) = f_r^{\text{dielectric}}(\omega_i, \omega_o) + f_t^{\text{dielectric}}(\omega_i, \omega_o), \quad (13)$$

$$f_r^{\text{dielectric}}(\omega_i, \omega_o) = \frac{F(\omega_i, \omega_{hr}) G_2(\omega_i, \omega_o, \omega_{hr}) D(\omega_{hr})}{4 |\omega_i \cdot \omega_g| |\omega_o \cdot \omega_g|}, \quad (14)$$

$$f_t^{\text{dielectric}}(\omega_i, \omega_o) = \frac{|\omega_i \cdot \omega_{ht}| |\omega_o \cdot \omega_{ht}|}{|\omega_i \cdot \omega_g| |\omega_o \cdot \omega_g|} + \frac{n_o^2 (1 - F(\omega_i, \omega_{ht})) G_2(\omega_i, \omega_o, \omega_{ht}) D(\omega_{ht})}{(n_i(\omega_i \cdot \omega_{ht}) + n_o(\omega_o \cdot \omega_{ht}))^2}. \quad (15)$$

Rough Conductor Rough conductors are modeled using the same BRDF as rough dielectrics $f_r^{\text{cond}} = f_r^{\text{dielectric}}$, but without a transmissive component, i.e. $f_t^{\text{cond}} = 0$.

Rough Diffuse If the material is diffuse, then the distribution of visible normals is transformed into a distribution of outgoing directions by a *diffuse reflection* with the micro-BRDF

$$f_m^{\text{diffuse}}(\omega_m, \omega_i, \omega_o) = \frac{a}{\pi} \langle \omega_o, \omega_m \rangle, \quad (16)$$

where $a \in [0, 1]$ is albedo of the microsurface. The rough diffuse BRDF then becomes

$$f^{\text{diffuse}}(\omega_i, \omega_o) = \frac{a}{\pi \cos \theta_o} \int_{\Omega} \langle \omega_o, \omega_m \rangle \frac{G_2(\omega_i, \omega_o, \omega_m)}{G_1(\omega_i, \omega_o, \omega_m)} D_{\omega_i}(\omega_m) d\omega_m. \quad (17)$$

Note that, in general, this equation has no analytic solution. Heitz and Dupuy [2015] propose an unbiased estimator computed by generating samples ω_m from D_{ω_i} and evaluating the diffuse micro-BRDF for these normals.

4 Insight and Overview

In this section, we develop an intuition for establishing the link between the Smith shadowing function, microsurface multiple scattering, and volumetric scattering in microflake volumes. We imagine a scattering volume enclosing the random surface and consider how to trace explicit depths, microfacets, reflections and subsequent intersections within the volume so as to produce transport that is consistent with the Smith model. We begin by recalling why multiple scattering is missing from most BSDFs and how the shadowing function is related to attenuation in classical volumetric transport.

Shadowing and Multiple Scattering in Microfacet Theory Microfacet BSDFs represent the set of outgoing directions for a ray *after leaving the microsurface*. Hence, they have to model all intersections and scattering on the microsurface. Because multiple scattering is difficult to model, classic models simply set the multiple-scattering contribution to 0 by using a shadowing function (Fig. 3).

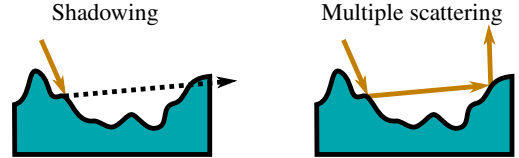


Figure 3: The shadowing function on microsurfaces.

Shadowing and Multiple Scattering in Microflake Theory An interesting observation is that microflake phase functions incorporate a “Smith-like” masking function through the normalization of the distribution of visible normals D_{ω_i} (as in Eq. 10), but do not incorporate shadowing [Heitz et al. 2015]. This is because multiple scattering inside the microflake medium is accounted for by the volumetric integrator, as illustrated in Fig. 4. Hence, microflake phase functions represent the distribution of outgoing directions directly after one interaction and *before leaving the medium* and before considering further intersections and scattering in the medium. The shadowing function on microsurfaces is thus equivalent to the volumetric attenuation that is sampled by the volumetric integrator.

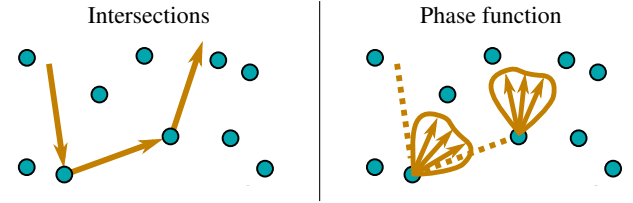


Figure 4: Multiple scattering in microflake volumes.

Our Smith Multiple-Scattering Model The primary observation behind our model is that the Smith microsurface model is equivalent to an inhomogeneous microflake volume with a free-path distribution (Sec. 5) and a phase function without shadowing (Sec. 6). Our model accounts for multiple scattering on microsurfaces analogous to volumetric scattering, by repeatedly tracing rays until an exit event is sampled (Fig. 5). We define the multiple-scattering BSDF as the expectation of these random walks (Sec. 7 and 8).

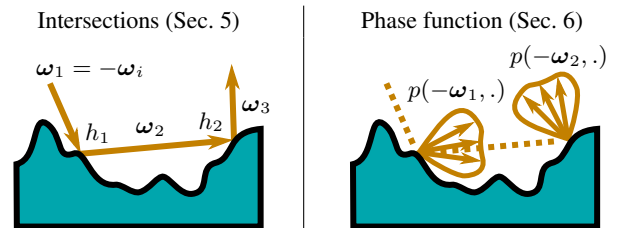


Figure 5: Multiple scattering on microsurfaces (Sec. 7 and 8).

5 Intersection with the Microsurface

The first milestone of our multiple-scattering model is the ability to track the heights h_r of the multiple intersections on the microsurface, as illustrated in Fig. 6. In this section, we show that the scattering on a Smith microsurface can be modeled with the equation of volumetric scattering, i.e. by means of an extinction coefficient σ_t (Sec. 5.1) and a free-path distribution that depends on it (Sec. 5.2). We will see that the resulting medium has all of the properties expected of a heightfield (Sec. 5.3).

Configuration In this section, we derive the intersection model for a ray traveling in direction ω_r of slope $\cot \theta_r$, starting at abscissa $\tau = 0$ and height h_r , and a target height h_{r+1} , as illustrated in Fig. 6.

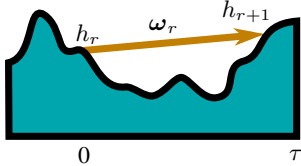


Figure 6: Intersection with the microsurface.

5.1 The Microsurface Extinction Coefficient

In this section, we propose a construction of the Smith volumetric extinction coefficient σ_t^{Smith} based on microflake theory [Jakob et al. 2010; Heitz et al. 2015] with an additional constraint to enforce a surface-like interface.

Non-Uniform Microsurface Density In a microflake volume, the presence of matter at some point is described by density $\rho^{\text{microflake}}$. Similarly, the presence of the microsurface at some height is described by the height PDF P^1 . However, in the Smith model, we assume a heightfield microsurface that is always below the ray. For a ray at height h , we know that the microsurface is located in $(-\infty, h]$ and the microsurface density is thus given by the conditional height PDF

$$\rho^{\text{Smith}}(h') = P^1(h' | h' \leq h) = \frac{\chi^+(h' \leq h) P^1(h')}{C^1(h)}. \quad (18)$$

producing an inhomogeneous microsurface density at a given ray height h ,

$$\rho^{\text{Smith}}(h) = \frac{P^1(h)}{C^1(h)}. \quad (19)$$

Microfacet Projected Area In a microflake volume, a ray traveling *towards* direction ω_r can intersect only microflakes such that $\langle -\omega_r, \omega_m \rangle > 0$. The probability of interaction increases with the projected area $\sigma^{\text{microflake}}(\omega_r)$ of the microflakes onto $-\omega_r$:

$$\sigma^{\text{microflake}}(\omega_r) = \int_{\Omega} \langle -\omega_r, \omega_m \rangle D(\omega_m) d\omega_m. \quad (20)$$

Note that $\sigma^{\text{microflake}}(\omega_r) = \sigma^{\text{microflake}}(-\omega_r)$ because microflake distributions are symmetric, i.e. $D(\omega_m) = D(-\omega_m)$. However, this is not the case for microfacet distributions. In Appendix B, we show

that the function Λ from the Smith model is such that

$$\begin{aligned} \sigma^{\text{Smith}}(\omega_r) &= \int_{\Omega} \langle -\omega_r, \omega_m \rangle D(\omega_m) d\omega_m \\ &= \Lambda(\omega_r) \cos \theta_r, \end{aligned} \quad (21)$$

$$\begin{aligned} \sigma^{\text{Smith}}(-\omega_r) &= \int_{\Omega} \langle \omega_r, \omega_m \rangle D(\omega_m) d\omega_m \\ &= (1 + \Lambda(\omega_r)) \cos \theta_r. \end{aligned} \quad (22)$$

Microsurface Extinction Coefficient In the volumetric microflake framework, the extinction coefficient is proportional to the volume density and the projected area of the microflakes

$$\sigma_t^{\text{microflake}}(\omega_r) = \rho^{\text{microflake}} \sigma^{\text{microflake}}(\omega_r). \quad (23)$$

For the same reason, the extinction coefficient in the Smith microsurface model is given by the density of the microsurface multiplied by the projected area of the microfacets:

$$\begin{aligned} \sigma_t^{\text{Smith}}(\omega_r, h) &= \rho^{\text{Smith}}(h) \sigma^{\text{Smith}}(\omega_r) \\ &= \Lambda(\omega_r) \cos \theta_r \frac{P^1(h)}{C^1(h)}. \end{aligned} \quad (24)$$

Fig. 7 illustrates σ_t^{Smith} for different incident directions.

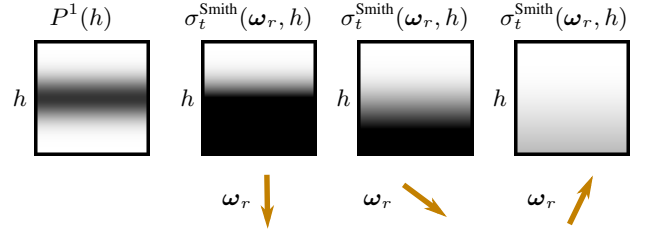


Figure 7: The microsurface extinction coefficient for varying incident directions ω_r .

5.2 The Microsurface Free Path

Microsurface Intersection Probability Being a classical microflake volume, the intersection probability densities at distances τ and $\tau + d\tau$ are uncorrelated. Consequently, the probability that there is no intersection in $[0, \tau]$ decreases exponentially with the integral of the extinction coefficient:

$$\begin{aligned} G_1^{\text{dist}}(\omega_r, h_r, \tau) &= \exp \left(- \int_0^\tau \sigma_t^{\text{Smith}}(\omega_r, h_r + \tau' \cot \theta_r) \left\| \frac{\partial d}{\partial \tau} \right\| d\tau' \right) \\ &= \left(\frac{C^1(h_r)}{C^1(h_r + \tau \cot \theta_r)} \right)^{\Lambda(\omega_r)} = \left(\frac{C^1(h_r)}{C^1(h_{r+1})} \right)^{\Lambda(\omega_r)}, \end{aligned} \quad (25)$$

where $\left\| \frac{\partial d}{\partial \tau} \right\|$ is the Jacobian of the abscissa parametrization¹. This probability $G_1^{\text{dist}}(\omega_r, h_r, \tau)$ is the masking function at distances in the interval $[0, \tau]$. The masking function from Eq. (1) is the limit at ∞ :

$$G_1^{\text{dist}}(\omega_r, h_r, \infty) = G_1^{\text{dist}}(\omega_r, h_r). \quad (26)$$

¹The distance d traveled by the ray depends on the angle θ_r : $d = \sqrt{\tau^2 + (\tau \cot \theta_r)^2} = \frac{\tau}{\sin \theta_r}$. We account for this in the density integral by multiplying by the parametrization Jacobian $\left\| \frac{\partial d}{\partial \tau} \right\| = \frac{1}{\sin \theta_r}$. Note that the Smith [1967] g function is the product $g = \sigma_t^{\text{Smith}} \left\| \frac{\partial d}{\partial \tau} \right\|$.

Free-Path Distribution The free-path CDF $C_{h_r, \omega_r}^1(h_{r+1})$ can be regarded as the microsurface CDF C^1 modified by the visibility due to the ray starting at position h_r and traveling in direction ω_r . It is defined by the probability that there is an intersection in $[0, \tau]$ and is given by

$$C_{h_r, \omega_r}^1(h_{r+1}) = \begin{cases} 0 & \text{if } \tau < 0 \\ 1 - G_1^{\text{dist}}(\omega_r, h_r, \tau) & \text{if } 0 \leq \tau < \infty \\ 1 & \text{if } \tau = \infty, \end{cases} \quad (27)$$

where $\tau = \infty$ represents the ray leaving the microsurface without intersecting it. In Appendix C, we provide the derivation of the associated free-path PDF

$$P_{h_r, \omega_r}^1(h_{r+1}) = \begin{cases} 0 & \text{if } h_{r+1} < h_r \text{ and } \theta_r < \frac{\pi}{2} \\ 0 & \text{if } h_{r+1} > h_r \text{ and } \theta_r > \frac{\pi}{2} \\ |\Lambda(\omega_r)| P^1(h_{r+1}) \frac{C^1(h_r)^{\Lambda(\omega_r)}}{C^1(h_{r+1})^{1+\Lambda(\omega_r)}} \\ + G_1^{\text{dist}}(\omega_r, h_r, \infty) \delta_\infty(h_{r+1}), \end{cases} \quad (28)$$

which can also be called the *distribution of visible heights*. The Dirac delta distribution δ_∞ accounts for the probability $G_1^{\text{dist}}(\omega_r, h_r, \infty)$ that the ray does not intersect the surface. An example of this PDF is illustrated in Fig. 8.

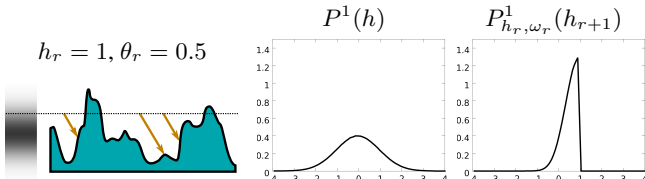


Figure 8: The free-path PDF (or “distribution of visible heights”).

Free-Path Sampling To sample an intersection between the microsurface and a ray starting from height h_{r+1} and traveling in direction ω_r , we generate a sample in the PDF P_{h_r, ω_r}^1 . To achieve this, we invert the CDF from Eq. (27). The first observation is that there is a probability $G_1^{\text{dist}}(\omega_r, h_r, \infty)$ that the ray will leave the microsurface without intersecting it. We generate a uniform random number \mathcal{U} and if $\mathcal{U} \leq G_1^{\text{dist}}(\omega_r, h_r, \infty)$ then the ray leaves the microsurface and $\tau = \infty$. Otherwise, we find τ such that

$$\mathcal{U} = C_{h_r, \omega_r}^1(h_{r+1}) = 1 - G_1^{\text{dist}}(\omega_r, h_r, \tau). \quad (29)$$

By multiplying the distance τ by the slope $\cot \theta_r$ of the ray direction we obtain the next height

$$h_{r+1} = C^{-1} \left(\frac{C^1(h_r)}{(1-\mathcal{U})^{1/\Lambda(\omega_r)}} \right). \quad (30)$$

We provide a proof of this result in Appendix D. Our height sampling procedure is summarized in Alg. 1.

Algorithm 1 Sample height $h_{r+1}(\omega_r, h_r, \mathcal{U})$

```

if  $\mathcal{U} \geq 1 - G_1^{\text{dist}}(\omega_r, h_r, \infty)$  then      ▷ Leave the microsurface
     $h_{r+1} = \infty$ 
else
     $h_{r+1} = C^{-1} \left( \frac{C^1(h_r)}{(1-\mathcal{U})^{1/\Lambda(\omega_r)}} \right)$  ▷ Intersect the microsurface
end if
return  $h_{r+1}$ 

```

5.3 Properties of the Microsurface Intersection Model

Table 3 highlights several important properties of our medium’s path sampling and we can see that they match properties expected

from a heightfield. For instance, rays traveling downwards ($\theta_r > \frac{\pi}{2}$) always intersect the microsurface and they cannot go below the lowest point of the surface at height $C^{-1}(0)$, while there is always a probability for rays to escape finite, classic volumetric media, even with high density. Another example is that rays traveling perfectly upwards ($\theta_r = 0$) always leave the microsurface without intersecting it, which is expected from a heightfield.

θ_r	ω_r	$\rho_{\text{Smith}}^{\text{Smith}}$ σ_t^{Smith}	h_{r+1}	interpretation
0	\uparrow	0	∞	the ray leaves the microsurface
$< \frac{\pi}{2}$	\nearrow	decrease with τ	$[h_r, C^{-1}(1)]$ or ∞	the ray moves away from the microsurface
$= \frac{\pi}{2}$	\rightarrow	constant	h_r	the ray stays at the same height
$> \frac{\pi}{2}$	\searrow	increase with τ	$[C^{-1}(0), h_r]$	the ray approaches the microsurface

Table 3: Properties of the microsurface intersection model.

6 Phase Function of the Microsurface

The second milestone of our multiple-scattering model is to compute how the light is scattered by the microsurface at the intersection points. In the previous section, we computed the intersections with the microsurface using the volumetric microflake framework. We now continue with this analogy and model how light is scattered by the visible microflakes (Sec. 6.1). This results in a microflake phase function (Sec. 6.2) similar to the generic microfacet BSDF from Eq. (11) and with all of the expected properties of microflake phase functions (Sec. 6.3).

Configuration We now model how light traveling along a direction ω_r is scattered at an intersection point, as illustrated in Fig. 9. In order to use the common notation for phase functions $p(\omega_i, \omega_o) = p(-\omega_r, \omega_o)$ (without reversing signs), we now set $\omega_i = -\omega_r$. Note that in all other sections, ω_i denotes the first incident direction $\omega_1 = -\omega_i$.

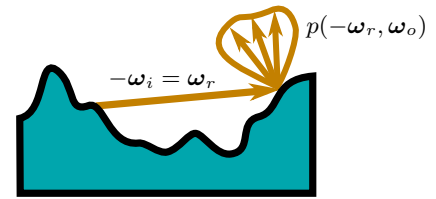


Figure 9: Phase function on the microsurface.

Observations It is important to note that p does not represent the scattering at exactly one point on the microsurface (i.e. of only one microfacet), but instead the average scattering at *all* microfacets that can potentially be intersected by the ray at this point of the microsurface. As normals are independent of heights on the Smith microsurface, there is no a priori information regarding the normal ω_m at an intersection point besides that it is visible to the ray, i.e. $\omega_i \cdot \omega_m > 0$.

Another observation is that p is a microflake phase function and not a microfacet BSDF. Unlike a BSDF, it does not represent the scattering of a geometric surface patch. In the example shown in Fig. 6, the ray is going upwards ($\theta_i > \frac{\pi}{2}$) and a BSDF model cannot be defined for such a configuration.

6.1 Distribution of Visible Normals

In the microflake framework, the definition of the distribution of visible normals (VNDF) is [Heitz et al. 2015]:

$$D_{\omega_i}(\omega_m) = \frac{\langle \omega_i, \omega_m \rangle D(\omega_m)}{\sigma^{\text{Smith}}(-\omega_i)}. \quad (31)$$

Using $\sigma^{\text{Smith}}(-\omega_i)$ from Eq. (22), the distribution of visible normals for any $\theta_i \in [0, \pi]$ becomes

$$D_{\omega_i}(\omega_m) = \frac{\langle \omega_i, \omega_m \rangle D(\omega_m)}{\cos \theta_i (1 + \Lambda(\omega_i))}, \quad (32)$$

which is the classic form of Eq. (10) defined for $\theta_i \leq \frac{\pi}{2}$. This confirms that the distribution of visible normals for the microsurface—derived within the microflake framework—yields the same result as the classic microfacet derivations. Furthermore, as we have verified that the definition of $\sigma^{\text{Smith}}(-\omega_i)$ is valid for any $\theta_i \in [0, \pi)$ (Sec. 5.1), we can now also use this definition of the VNDF for configurations where the ray goes upwards ($\theta_i > \frac{\pi}{2}$).

6.2 Derivation of the Phase Functions

Starting from the VNDF, we derive the microflake phase functions associated with different microsurface materials.

Generic Phase Function As shown by Heitz et al. [2015], the phase function for a distribution of visible normals D_{ω_i} and a micro-BSDF $f_m(\omega_i, \omega_o, \omega_m)$ is

$$p(\omega_i, \omega_o) = \int_{\Omega} f_m(\omega_m, \omega_i, \omega_o) \langle \omega_o, \omega_m \rangle D_{\omega_i}(\omega_m) d\omega_m, \quad (33)$$

which is the cosine-weighted BSDF of the generic, rough material from Eq. (11) without the shadowing function. The generic procedure to importance sample the phase functions is to sample a normal ω_m from D_{ω_i} , and an outgoing direction ω_o from the cosine-weighted micro-BSDF $f_m(\omega_i, \omega_o, \omega_m) \cos \theta_o$.

Algorithm 2 Sample generic phase function

```
 $\omega_m \leftarrow \text{sample } D_{\omega_i}$ 
 $(w, \omega_o) \leftarrow \text{sample } f_m(\omega_i, \omega_o, \omega_m) \cos \theta_o$ 
```

Dielectric Phase Function Inserting the dielectric micro-BSDF from Eq. (12) into Eq. (33), and expanding D_{ω_i} from Eq. (32) yields

$$\begin{aligned} p^{\text{dieel}}(\omega_i, \omega_o) &= \frac{F(\omega_i, \omega_{hr}) D_{\omega_i}(\omega_{hr})}{4 |\omega_i \cdot \omega_{hr}|} \\ &+ \langle \omega_o, \omega_m \rangle \frac{\eta_o^2 (1 - F(\omega_i, \omega_{ht})) D_{\omega_i}(\omega_{ht})}{(\eta_i (\omega_i \cdot \omega_h) + \eta_o (\omega_o \cdot \omega_h))^2}. \end{aligned} \quad (34)$$

To importance sample p^{dieel} , we sample a normal ω_m from D_{ω_i} , then choose to perform either a specular reflection or refraction with a probability equal to the Fresnel term [Walter et al. 2007]; the weight of the sample is $w = 1$ (Alg. 3).

Algorithm 3 Sample dielectric phase function

```
 $\omega_m \leftarrow \text{sample } D_{\omega_i}$ 
 $\text{if } \mathcal{U} < F(\omega_i, \omega_m) \text{ then}$ 
     $\omega_o \leftarrow \text{reflect}(\omega_i, \omega_m)$   $\triangleright$  outgoing direction
 $\text{else}$ 
     $\omega_o \leftarrow \text{transmit}(\omega_i, \omega_m)$   $\triangleright$  outgoing direction
 $\text{end if}$ 
 $w \leftarrow 1$   $\triangleright$  weight
```

Conductor Phase Function Conductor materials can be handled similar to dielectrics but without transmission:

$$p^{\text{cond}}(\omega_i, \omega_o) = \frac{F(\omega_i, \omega_{hr}) D_{\omega_i}(\omega_{hr})}{4 |\omega_i \cdot \omega_{hr}|}. \quad (35)$$

To importance sample p^{cond} , we sample a normal ω_m from D_{ω_i} , apply the reflection operator, and the weight of the sample is $w = F(\omega_i, \omega_m)$ (shown in Alg. 4).

Algorithm 4 Sample conductor phase function

$\omega_m \leftarrow \text{sample } D_{\omega_i}$	\triangleright outgoing direction
$\omega_o \leftarrow \text{reflect}(\omega_i, \omega_m)$	\triangleright weight
$w \leftarrow F(\omega_i, \omega_m)$	

Diffuse Phase Function By inserting the diffuse micro-BSDF from Eq. (16) into Eq. (33) and expanding D_{ω_i} from Eq. (32) we obtain

$$p^{\text{diff}}(\omega_m, \omega_i, \omega_o) = \frac{a}{\pi} \int_{\Omega} \langle \omega_o, \omega_m \rangle D_{\omega_i}(\omega_m) d\omega_m, \quad (36)$$

which has no closed-form evaluation. An unbiased estimator is obtained by sampling a normal ω_m from D_{ω_i} and evaluating $\frac{a}{\pi} \langle \omega_o, \omega_m \rangle$ as proposed by Heitz et al. [2015] (Alg. 5).

Algorithm 5 Stochastic evaluation of diffuse phase function

$\omega_m \leftarrow \text{sample } D_{\omega_i}$	
$\text{return } \frac{a}{\pi} \langle \omega_o, \omega_m \rangle$	\triangleright weight

To importance sample f_p^{diff} , we sample a normal ω_m from D_{ω_i} and next a diffusely reflected direction ω_o in the hemisphere of ω_m (shown in Alg. 6).

Algorithm 6 Sample diffuse phase function

$\omega_m \leftarrow \text{sample } D_{\omega_i}$	
$\omega_o \leftarrow \text{diffuse}(\omega_i, \omega_m)$	\triangleright outgoing direction
$w \leftarrow a$	\triangleright weight

6.3 Properties of the Phase Functions

Since we derived the phase function p from the equations of the microflake framework, it inherits the expected, associated properties.

Reciprocity Microfacet BSDFs are reciprocal, i.e. all terms associated with ω_i have their counterpart associated with ω_o . However, we have seen that p accounts for masking towards ω_i (which is the normalization factor of D_{ω_i}), but it does not incorporate shadowing towards ω_o . It is thus non-reciprocal in the sense of microfacet BSDFs, but it is reciprocal in the sense of microflake phase functions, which satisfy the following reciprocity constraint:

$$\sigma^{\text{microflake}}(\omega_i) p(\omega_i, \omega_o) = \sigma^{\text{microflake}}(\omega_o) p(\omega_o, \omega_i). \quad (37)$$

As explained in Sec. 5.1, the function σ^{Smith} is not symmetric and we need to account for the sign:

$$\sigma^{\text{Smith}}(-\omega_i) p(\omega_i, \omega_o) = \sigma^{\text{Smith}}(-\omega_o) p(\omega_o, \omega_i). \quad (38)$$

By expanding $\sigma^{\text{Smith}}(-\omega_i)$ from Eq. (22) we obtain the Smith phase function reciprocity constraint:

$$(1 + \Lambda(\omega_i)) \cos \theta_i p(\omega_i, \omega_o) = (1 + \Lambda(\omega_o)) \cos \theta_o p(\omega_o, \omega_i). \quad (39)$$

The phase functions p^{dieel} , p^{cond} and p^{diff} derived in Sec. 6.2 satisfy this property.

Energy Conservation A microflake phase function is energy conserving, i.e.

$$\int_{\Omega} p(\omega_i, \omega_o) d\omega_o = 1, \quad (40)$$

if the micro-BRDF f_m from which it is derived represents a non-absorptive material. A dielectric microsurface is always non-absorptive because all of the energy is either reflected or transmitted and $p^{\text{dielectric}}$ is energy conserving. A conductor microsurface is non-absorptive only if all of the energy is reflected (i.e. if the Fresnel term equals 1), and a diffuse microsurface is non-absorptive if the albedo equals 1.

7 Random Walk on the Microsurface

In this section, we explain how to simulate a random walk on a microsurface using the height sampling procedure of Sec. 5.2 and the phase function sampling of Sec. 6.2. We first focus on reflective microsurfaces (conductor and diffuse), then discuss transmission (dielectric). The random walk is implemented by Alg. 7 and illustrated in Fig. 10.

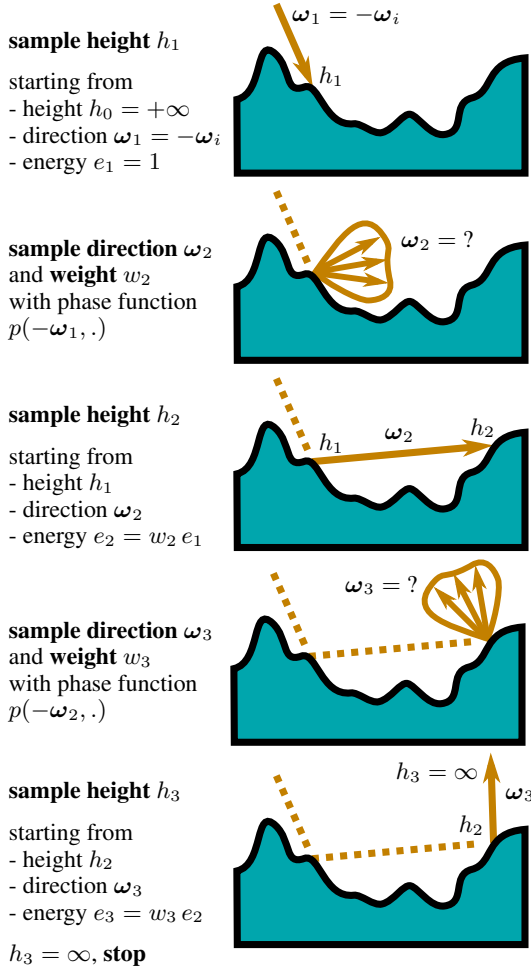


Figure 10: Illustration of a random walk on a statistical microsurface. The ray scatters on the microsurface until it leaves. Each scattering event is defined by its height h_r and its direction ω_r .

Variables and Initialization During the random walk, our algorithm tracks the following variables for each intersection point n :

- the height of the intersection point h_r ,
- the direction of the ray before the intersection ω_r ,
- and the energy throughput of the ray e_r .

The initial energy throughput is $e_1 = 1$, the initial height, before the first intersection, is set to $h_0 = \infty$, and the initial ray direction is the incident direction $\omega_1 = -\omega_i$.

Multiple Scattering Loop After initialization, the algorithm performs the random walk until the ray leaves the surface. In each iteration, the following steps are executed:

- **sample height:** we use Alg. 1 to sample a height h_r given the previous height h_{r-1} and the ray direction ω_r .
- **leaving the microsurface:** if $h_r = \infty$, the ray leaves the microsurface and the loop is terminated.
- **sample direction:** we use the sampling algorithm associated with the phase function $p(-\omega_r, .)$ (Sec. 6.2) to determine the new ray direction ω_{r+1} and its sampling weight w_{r+1} .
- **update throughput:** the energy throughput of the light path is updated by multiplying it by the weight of the sample: $e_{r+1} = w_{r+1} e_r$.

Algorithm 7 Random Walk

```

 $h_0 \leftarrow \infty$                                  $\triangleright$  initial height
 $e_1 \leftarrow 1$                                   $\triangleright$  initial energy
 $\omega_1 \leftarrow -\omega_i$                           $\triangleright$  initial direction
 $r \leftarrow 1$                                    $\triangleright$  initial index

while true do
     $h_r \leftarrow \text{sample}(h_{r-1}, \omega_r)$            $\triangleright$  next height
    if  $h_r = \infty$  then                             $\triangleright$  leave microsurface?
        break
    end if
     $(\omega_{r+1}, w_{r+1}) \leftarrow \text{sample } p(-\omega_r, .)$        $\triangleright$  next direction
     $e_{r+1} \leftarrow w_{r+1} e_r$                            $\triangleright$  next energy
     $r \leftarrow r + 1$ 
end while

```

Note on Dielectrics The above description assumes that rays always scatter above the interface, i.e. outside the material. However, if the material is dielectric, the ray can cross the interface and scatter inside. If P^1 is symmetric, we account for the correct intersection probabilities when the ray scatters inside by flipping the configuration vertically, as shown in Fig. 11.

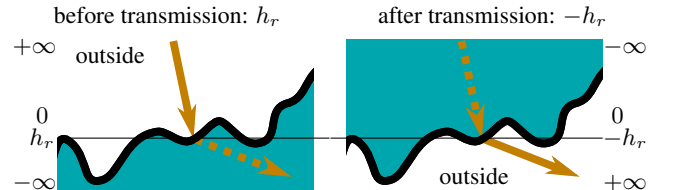


Figure 11: Vertical flip. After each transmission event, we vertically flip the configuration to track the correct values.

8 The Multiple-Scattering BSDF

In this section, we define the properties associated with one random walk (Sec. 8.1). We then define the multiple-scattering BSDF of the Smith model as the expectation of random walks (Sec. 8.2) and we show that this BSDF model has all of the physical properties expected from a BSDF (Sec. 8.3).

8.1 Properties of One Random Walk

Definition A random walk is described by a sequence of N heights, directions and energy throughputs $[(\omega_1, h_1, e_1), \dots, (\omega_N, h_N, e_N)]$; an example is illustrated in Fig. 12.

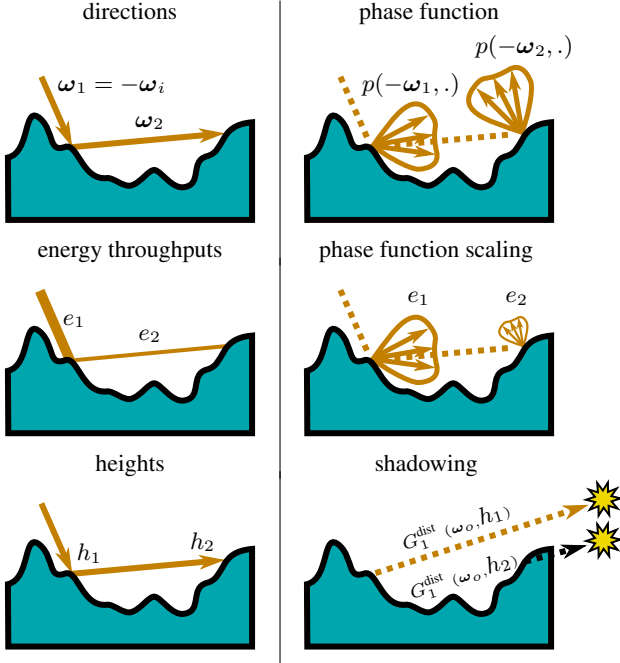


Figure 12: Random walk description.

Distribution We use $E_r(\omega_o)$ to denote the contribution of the r -th bounce to the energy scattered outside the microsurface, i.e. in direction ω_o . It depends on the energy throughput e_r , the phase function $p(-\omega_r, \omega_o)$ and the probability that the point at height h_r is not shadowed from direction ω_o , i.e. on the shadowing function $G_1^{\text{dist}}(\omega_o, h_r)$:

$$E_r(\omega_o) = e_r p(-\omega_r, \omega_o) G_1^{\text{dist}}(\omega_o, h_r). \quad (41)$$

The total scattered energy by a random walk of length N is the sum of the energies contributed at each bounce (Eq. (41)):

$$\begin{aligned} E_{1,\dots,N}(\omega_o) &= \sum_{r=1}^N E_r(\omega_o) \\ &= \sum_{r=1}^N e_r p(\omega_r, \omega_o) G_1^{\text{dist}}(\omega_o, h_r). \end{aligned} \quad (42)$$

Properties As expected from a single sample generated with a Monte Carlo technique, the distribution of scattered energy of a single random walk $E_{1,\dots,N}$ is not a BSDF nor a phase function and it is non-reciprocal and non-energy conserving. However, in the next section we will see that the expectation of the random walks is the physically correct multiple-scattering BSDF.

8.2 Definition of the Multiple-Scattering BSDF

In this section, we define the multiple-scattering BSDF. Intuitively, a multiple-scattering BSDF represents how energy is distributed after scattering on the microsurface on a macroscopic scale (“on average”). This average is the BSDF of our multiple-scattering model.

Definition The multiple scattering BSDF f is the average of the random walk distributions $E_{1,\dots,N}$ from Eq. (42):

$$\begin{aligned} f(\omega_i, \omega_o) \cos \theta_o &= \mathbb{E} \left[\sum_{r=1}^N E_{1,\dots,N}(\omega_o) \right] \\ &= \mathbb{E} \left[\sum_{r=1}^N e_r p(\omega_r, \omega_o) G_1^{\text{dist}}(\omega_o, h_r) \right], \end{aligned} \quad (43)$$

where $\mathbb{E}[\cdot]$ denotes the expectation over the space of the random walks, which is parameterized by the random numbers used to generate the random walks in Alg. 7.

8.3 Properties of the Multiple-Scattering BSDF

In this section, we show that the multiple-scattering BSDF from Eq. (43) is a valid BSDF with all of the expected physical properties.

Reciprocity The BSDF in Eq. (43) is reciprocal:

$$f(\omega_i, \omega_o) = f(\omega_o, \omega_i). \quad (44)$$

Since the microsurface light transport modeled in Sec. 5 and 6 is reciprocal, the emerging light transport is also reciprocal by construction. Please refer to our supplemental material where we provide our implementation for experimental verification.

Energy Conservation If the surface is non-absorptive then the multiple-scattering BSDF from Eq. (43) is energy conserving, i.e.

$$\int_{\Omega} f(\omega_i, \omega_o) \cos \theta_o d\omega_o = 1. \quad (45)$$

In Sec. 8.1 we discussed that individual random walks $E_{1,\dots,N}$ can potentially integrate to values greater than 1 as they can account for the energy of a multitude of interactions. On average, however, this is exactly counterbalanced by the energy loss due to the shadowing, G_1^{dist} , which is a factor in E_r (Eq. (41)): the energy loss due to shadowing for one direction is $1 - G_1^{\text{dist}}$ and after each interaction, the probability of intersecting the microsurface in the same direction again and obtaining an additional distribution E_r is precisely $1 - G_1^{\text{dist}}$. Hence, the energy loss at one interaction due to shadowing exactly corresponds to the energy surplus of random walks with further interactions. Again, this property can be verified experimentally using our implementation in the supplemental material.

Consistency with Closed-Form Single Scattering The formulation of the multiple-scattering BSDF from Eq. (43) is a direct extension of the classic single-scattering model reviewed in Sec. 3.2. In fact, if we compute the average over the random walks for $N = 1$ (one interaction only) we get the classic single-scattering BSDF model from Eq. (11):

$$\begin{aligned} f(\omega_i, \omega_o) \cos \theta_o &= \mathbb{E}[E_1(\omega_o)] \\ &= \mathbb{E}[e_1 p(-\omega_1, \omega_o) G_1^{\text{dist}}(\omega_o, h_1)]. \end{aligned} \quad (46)$$

9 Implementation in a Rendering Engine

Integrating a material into a rendering system typically requires the implementation of three functions: evaluation, importance sampling, and the PDF of the importance sampling procedure, which is required when *multiple importance sampling* (MIS) is used to reduce variance.

Importance Sampling We directly use Alg. 7 to importance sample the BSDF, i.e. to determine an outgoing direction when the ray scatters on the microsurface until it leaves it. The weight associated with this sample is the final energy throughput e_r . If the material is non-absorptive, then $e_r = 1$ and the importance sampling technique is perfect.

Evaluation There is no closed-form evaluation of our BSDF. Instead, each time the evaluation is required, we compute a new random walk and evaluate $E_{1,\dots,N}$ from Eq. (42). This provides an unbiased estimate of the BSDF.

PDF Evaluating the PDF for importance sampling causes similar difficulties as the evaluation, as there is no closed-form evaluation. Furthermore, unlike for the BSDF, we cannot resort to a stochastic evaluation: computing an unbiased stochastic estimate of the PDF does not work as it is used in the denominator of the MIS weights. Indeed, division does not commute with averaging and doing so introduces bias in the result computed by MIS. Hence, we evaluate the classic PDF of the first scattering event and add a small diffuse contribution to account for the multiple scattering (set to 0.2 in our renderings).

9.1 Reducing Variance in the Stochastic Evaluation

We present optimizations that considerably lower the variance of the stochastic estimate of the BSDF.

Closed-Form for the Single-Scattering Term To improve the variance reduction, we replace the contribution of the first bounce $E_1 = e_1 p(-\omega_1, \omega_o) G_1(\omega_o, h_1)$ by the closed-form evaluation of the single-scattering term. This is equivalent to replacing the masking and shadowing functions evaluated at height h_1 by the average height-correlated masking-shadowing function G_2 and thus reducing the variance introduced by the sampling of h_1 . Note that this does not bias the results as the expectation of E_1 is effectively the closed-form single-scattering contribution.

Choosing the Incident Direction with Less Variance We use the random walks to evaluate an estimate of the BSDF $f(\omega_i, \omega_o)$. Since the BSDF is reciprocal, the expectation is the same if we start the random walk from either ω_i or ω_o . The distribution of visible heights, from which the height h_1 of the first intersection is sampled, has lower variance at grazing angles and high roughness (because the top of a rough microsurface is more visible). Hence, sampling from the direction that has the lowest incident angle and/or the largest projected roughness provides the best variance reduction. Because of the stretch-invariance property of the distribution of visible heights [Heitz 2014], its variance depends only on $\alpha_i \tan \theta_i$. Hence, we start the random walk from ω_i if $\alpha_i \tan \theta_i > \alpha_o \tan \theta_o$, and from ω_o otherwise.

Integrating Intersection Probability In Alg. 7, the intersection heights are sampled stochastically with probability $1 - G_1^{\text{dist}}(\omega_r, h_r, \infty)$. To remove the variance due to this stochastic sampling, we enforce the intersections and weight the

path with their probabilities. We use a random number $U \in [0, 1 - G_1^{\text{dist}}(\omega_r, h_r, \infty)]$ to sample the height of the next intersection given that there is an intersection. Doing so enforces the random walk to continue and we compensate for this by multiplying the energy of the sample by the probability of the intersection, i.e. we update: $e_{r+1} \leftarrow e_{r+1} (1 - G_1^{\text{dist}}(\omega_r, h_r, \infty))$. Note that with this modification we need a criterion to terminate the random walk. We terminate it when the remaining energy is below a small threshold or when the maximal number of bounces has been reached (see below).

Early Random Walk Termination We observed that the energy contributed by random walks of length 3 or above, $E_{3,\dots,N}$, is less than 0.002% for all *non-absorptive* materials presented in the paper using Beckmann or GGX roughnesses in $\alpha \in [0, 1]$. For absorptive materials, this contribution is even lower. For our renderings we thus terminate the random walk after the third interaction. Note that although this removes a small amount of the energy, it does not break the reciprocity of the model.

9.2 Limitations

Our BSDF has two limitations compared to traditional models.

Stochastic Evaluation The stochastic evaluation in the model is well-suited for Monte Carlo rendering but it introduces additional variance. However, as the closed-form evaluation can be used for the single-scattering contribution (as proposed above), variance is only introduced for the higher-order interactions.

Nevertheless, our model is unsuitable for real-time rendering where the shading has to be smooth with one sample per pixel.

Global Illumination Integrator Some integrators, most notably Metropolis Light Transport, may be less efficient with our stochastic random walk as they use a non-deterministic number of random values.

10 Results

Comparison against Simulated Data We compare the prediction of our model against simulated data. To collect such data, we create and raytrace instances of Beckmann surfaces, as illustrated in Fig. 13. We generate the Beckmann surface instances using the method of Heitz [2015]. In Fig. 14, we compare the predictions of our free-path PDF from Eq. (28) with the intersection distributions computed explicitly by the raytracing simulation. In Fig. 15, we compare the predictions of our multiple-scattering BSDF from Eq. (43) with the sets of outgoing directions computed explicitly by the raytracing simulation. For a large variety of roughnesses, anisotropy and inclinations we found our BSDF model to accurately predict both the albedo and angular distribution of exitant energy. Note that double scattering can account for 20% of the total reflectance or transmittance in some cases, making multiple scattering an essential component of microfacet BSDFs.

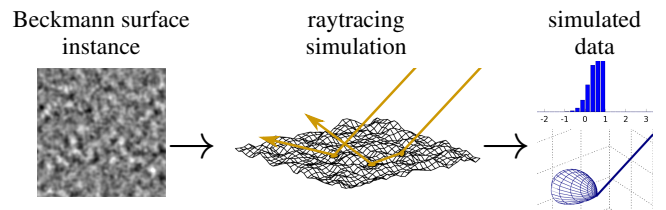


Figure 13: Collecting simulated data for comparison against our free-path model (Fig. 14) and multiple-scattering BSDF (Fig. 15).

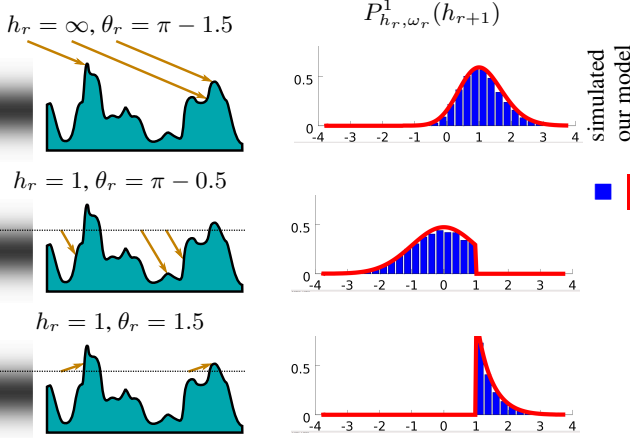


Figure 14: Comparison of our microsurface free-path model against simulated data. We obtained this data by raytracing a Beckmann surface instance ($\alpha = 1$). More results are available in our supplemental material.

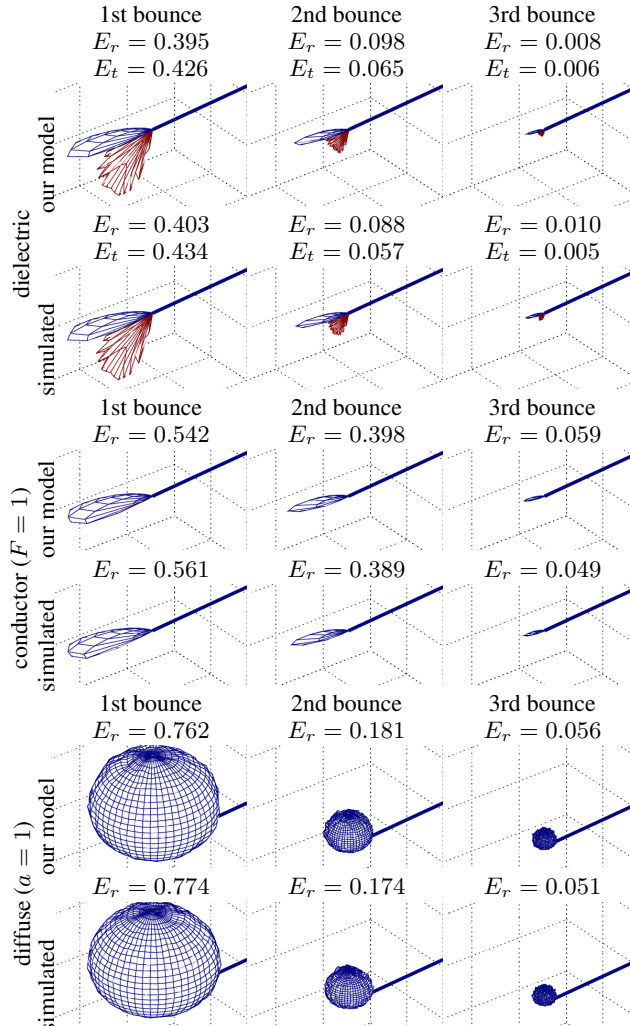


Figure 15: Comparison of our multiple-scattering BSDF model against simulated data. We obtained the data by raytracing an anisotropic Beckmann surface instance ($\alpha_x = 0.1, \alpha_y = 1.0$). The incident angle is $\theta_i = 1.5$. E_r and E_t denote the total amount of reflected and transmitted energies, respectively. More results are available in our supplemental material.

White Furnace Tests In Fig. 16, we provide renders of different microsurface materials lit by a constant white environment map, to demonstrate the energy conservation. Under this illumination, the object disappears if the albedo is one. This is the case for all of our microsurface materials if the microfacet material is not absorbing energy.

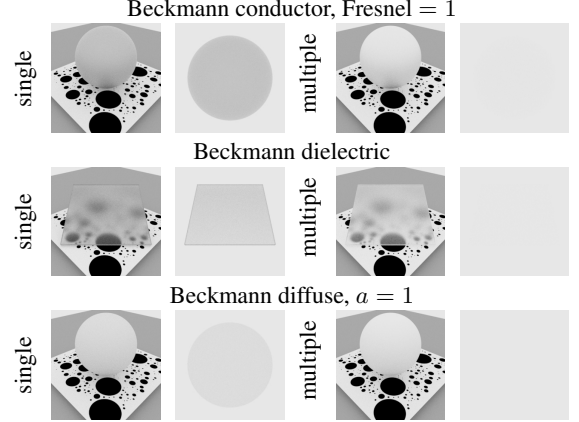


Figure 16: White furnace test for different microfacet materials.

Numerical Validation In our supplemental material, we describe a tutorial implementation and a set of unit tests we used to numerically validate the properties of the model: energy conservation, reciprocity, agreement between height sampling and masking-shadowing, agreement with the classic single-scattering BSDF, etc. We also show a comprehensive breakdown of the multiple-scattering interactions into groups based on the sequence of reflection (R) and transmission (T) events, such as TRT and TTR lobes, which are individually simple but sum to produce the complex lobes seen in the complete rough dielectric BSDF.

Practical Rendering We tested our new family of materials in a practical rendering setup and evaluated the visual contribution of multiple scattering. Fig. 17 shows a collection of bottles with different microfacet materials. Rough dielectrics in particular exhibit a large contribution from indirect bounces. Without multiple scattering, rough transmittance appears unnatural, which is hard to compensate for by tuning parameters, especially in the presence of textured roughness (see Figs. 1 and 20). Note that since we do not depend on any precomputed data, we fully support textured input, which is important for creating visually rich images. Also multiple scattering on rough conductors shows a significant impact on surface appearance, clearly visible in the difference image in Fig. 17 and in Fig. 18.

Performance The performance impact of using multiple scattering within the microsurface is significant and can almost double the render time, especially in the bottles scene (Fig. 17). Note that this depends on the roughness of the material as higher roughness will typically lead to more indirect bounces (also see the supplemental material for more information). Also, the difference image shows that a significant portion of the indirect light transport between different bottles is caused by multiple scattering *within* a microsurface. This reduced attenuation of light can lead to longer paths, since Russian roulette will not terminate these earlier.

Saturation Effects Since the absorption spectrum of the microfacet material is repeatedly multiplied by the illumination spectrum, multiple scattering within the microsurface saturates the color of the reflected radiance. This can be seen for a conductor in Fig. 18 and for diffuse microfacets in Fig. 19.

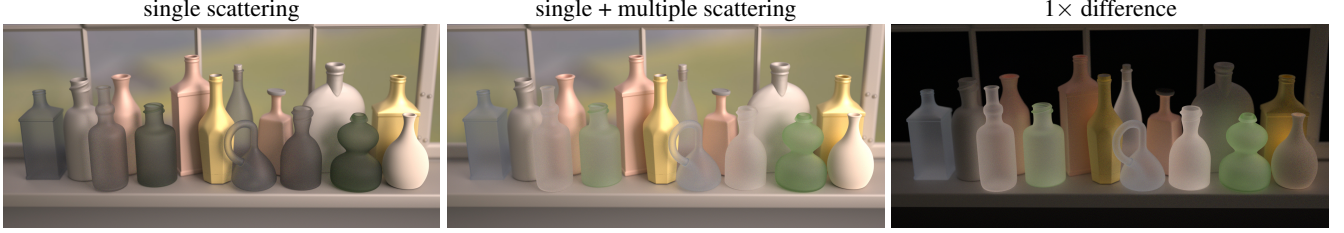


Figure 17: Rough bottles with microfacet materials. *The difference image has been computed in linear color space and converted to Adobe RGB, the same way as the multiple and single scattering renders. Most materials use a GGX slope distribution with $\alpha = 0.5$, the shinier ones use $\alpha = 0.3$. Computing the additional light transport seen in the difference image results in an increase in the render time of 87%.*

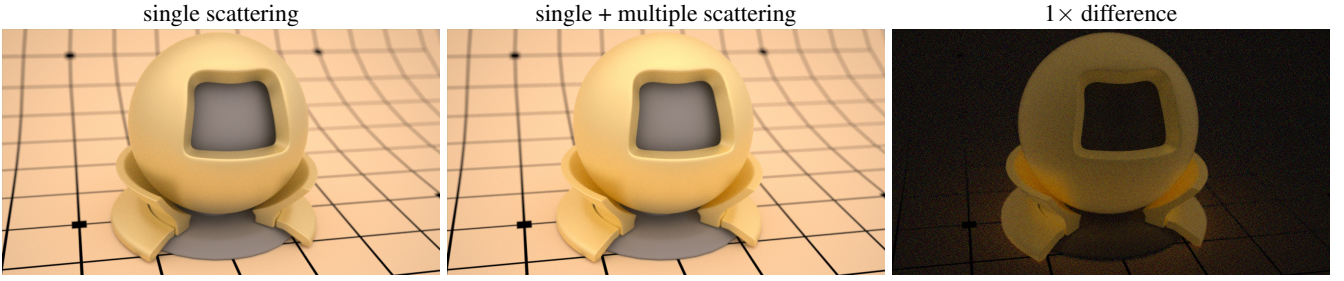


Figure 18: A rough conductor with a GGX normal distribution $\alpha = 0.3$ and a spectral gold Fresnel. *The color saturation increases notably with the addition of multiple scattering. The overall speed impact of the multiple-scattering BRDF was 24% total render time in this case.*

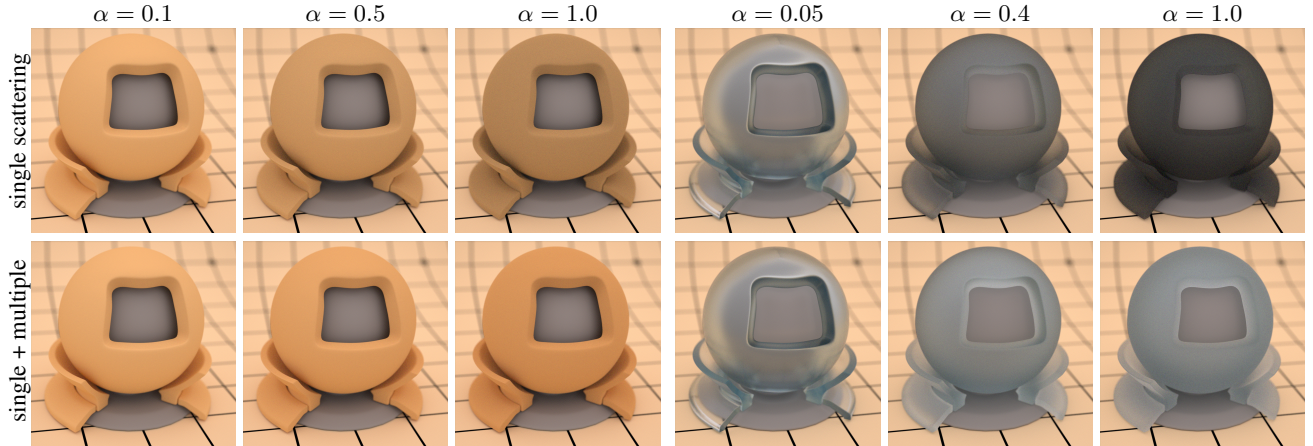


Figure 19: Rough diffuse and dielectric materials with GGX normal distribution. *The cost of the diffuse multiple-scattering BRDF is 6%, 50%, and 62% additional render time for roughnesses $\alpha = 0.1, 0.5$, and 1.0 , respectively. Instead of the typical darkening for rough single scattering materials, we observe color saturation at higher roughness. The albedo of the diffuse microfacet material used here in RGB is $(0.9, 0.5, 0.2)$. The performance for the dielectric is about the same for $\alpha = 0.05$ and all of the multiple-scattering images, and the single scattering $\alpha = 0.4$ and $\alpha = 1.0$ are about 2 \times and 3 \times faster, respectively, due to paths with low contribution terminating early.*

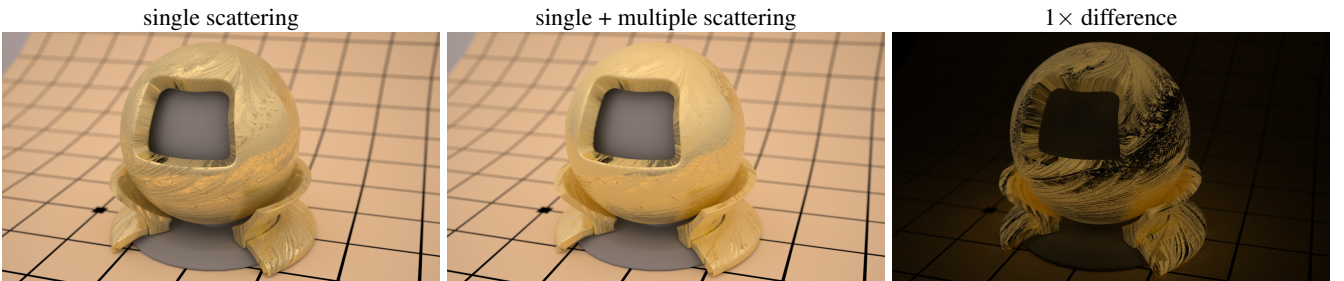


Figure 20: A conductor with a GGX normal distribution, textured roughness, and a spectral gold Fresnel. *With single scattering only, the surface albedo appears to be textured too, which is undesirable. Our analytic model allows for textured roughness and/or anisotropy and preserves the shiny appearance. The overall speed impact of the multiple-scattering BRDF was 27% total render time in this case.*

11 Conclusion

We have extended microfacet theory based on the Smith model to include microsurface multiple scattering at rough material interfaces for reflectance and transmission. We compared the predictions made by our model with results obtained by simulating multiple scattering on explicit microsurfaces generated with a noise primitive and they showed good agreement. In contrast to previous parametric BSDFs that considered only single-surface scattering, our new model is energy conserving and exhibits important saturated reflections for rough conductive surfaces. The core of our model is the derivation of a volumetric random walk model for Smith random surfaces. This model readily supports anisotropy and common normal distributions such as Beckmann and GGX. We have presented practical importance sampling and related methods for incorporating our model into a physically based renderer and have presented results demonstrating the visual impact of supporting microsurface multiple scattering in image synthesis.

Acknowledgements

The authors wish to thank Stephen Hill for carefully proofreading the paper and Károly Zsolnai-Fehér for creating and narrating the supplementary video. Thanks also to Joe Letteri for many inspiring conversations encouraging the volume interpretation of surfaces.

References

- BECKMANN, P., AND SPIZZICHINO, A. 1963. *The scattering of electromagnetic waves from rough surfaces*. International series of monographs on electromagnetic waves. Pergamon Press.
- BOURLIER, C., AND BERGINC, G. 2004. Multiple scattering in the high-frequency limit with second-order shadowing function from 2d anisotropic rough dielectric surfaces: I. theoretical study. *Waves in Random Media* 14, 3, 229–252.
- COOK, R. L., AND TORRANCE, K. E. 1982. A reflectance model for computer graphics. *ACM Transactions on Graphics* 1, 1 (Jan.), 7–24.
- FURFARO, R., AND GANAPOL, B. 2007. Spectral Theory for Photon Transport in Dense Vegetation Media: Caseology for the Canopy Equation. *Transport Theory and Statistical Physics* 36, 1, 107–135.
- HEITZ, E., AND D'EON, E. 2014. Importance sampling microfacet-based BSDFs using the distribution of visible normals. In *Proc. Eurographics Symposium on Rendering*, 103–112.
- HEITZ, E., AND DUPUY, J. 2015. Implementing a simple anisotropic rough diffuse material with stochastic evaluation. Research report.
- HEITZ, E., DUPUY, J., CRASSIN, C., AND DACHSBACHER, C. 2015. The SGGX microflake distribution. *ACM Transactions on Graphics (Proc. SIGGRAPH)* 34, 4, 48:1–48:11.
- HEITZ, E. 2014. Understanding the masking-shadowing function in microfacet-based BRDFs. *Journal of Computer Graphics Techniques* 3, 2, 32–91.
- HEITZ, E. 2015. Generating procedural Beckmann surfaces. Research report.
- HILL, S., MCAULEY, S., BURLEY, B., CHAN, D., FASCIONE, L., IWANICKI, M., HOFFMAN, N., JAKOB, W., NEUBELT, D., PESCE, A., AND PETTINEO, M. 2015. Physically based shading in theory and practice. In *ACM SIGGRAPH Courses*.
- JAKOB, W., ARBREE, A., MOON, J. T., BALA, K., AND MARSCHNER, S. 2010. A radiative transfer framework for rendering materials with anisotropic structure. *ACM Transactions on Graphics (Proc. SIGGRAPH)* 29, 4, 53:1–53:13.
- JAKOB, W., D'EON, E., JAKOB, O., AND MARSCHNER, S. 2014. A comprehensive framework for rendering layered materials. *ACM Transactions on Graphics (Proc. SIGGRAPH)* 33, 4, 118:1–118:14.
- KELEMEN, C., AND SZIRMAK-KALOS, L. 2001. A microfacet based coupled specular-matte brdf model with importance sampling. In *Eurographics short presentations*.
- KOENDERINK, J., VAN DOORN, A., DANA, K., AND NAYAR, S. 1999. Bidirectional reflection distribution function of thoroughly pitted surfaces. *International Journal of Computer Vision* 31, 2, 129–144.
- KUŠČER, I., AND SUMMERFIELD, G. C. 1969. Symmetries in scattering of slow neutrons. *Phys. Rev.* 188, 3 (Dec), 1445–1449.
- LI, H., PINEL, N., AND BOURLIER, C. 2011. A monostatic illumination function with surface reflections from one-dimensional rough surfaces. *Waves in Random and Complex Media* 21, 1, 105–134.
- LI, H., PINEL, N., AND BOURLIER, C. 2013. Polarized infrared reflectivity of one-dimensional gaussian sea surfaces with surface reflections. *Appl. Opt.* 52, 25 (Sep), 6100–6111.
- LI, H., PINEL, N., AND BOURLIER, C. 2014. Polarized infrared reflectivity of 2d sea surfaces with two surface reflections. *Remote Sensing of Environment* 147, 0, 145 – 155.
- OREN, M., AND NAYAR, S. K. 1995. Generalization of the lambertian model and implications for machine vision. *International Journal of Computer Vision* 14, 3, 227–251.
- PINEL, N., BOURLIER, C., AND SAILLARD, J. 2005. Energy conservation of the scattering from one-dimensional random rough surfaces in the high-frequency limit. *Opt. Lett.* 30, 15 (Aug), 2007–2009.
- RAAB, M., SEIBERT, D., AND KELLER, A. 2008. Unbiased global illumination with participating media. In *Monte Carlo and Quasi-Monte Carlo Methods 2006*, 591–606.
- SMITH, B. 1967. Geometrical shadowing of a random rough surface. *IEEE Transactions on Antennas and Propagation* 15, 668–671.
- STAM, J. 2001. An illumination model for a skin layer bounded by rough surfaces. In *Rendering Techniques*, 39–52.
- TORRANCE, K. E., AND SPARROW, E. M. 1967. Theory for off-specular reflection from roughened surfaces. *Journal of the Optical Society of America (JOSA)* 57, 9, 1105–1112.
- WALTER, B., MARSCHNER, S. R., LI, H., AND TORRANCE, K. E. 2007. Microfacet models for refraction through rough surfaces. In *Proc. Eurographics Symposium on Rendering*, 195–206.
- WILLIAMS, M. M. R. 1978. Transport theory in anisotropic media. In *Mathematical Proceedings of the Cambridge Philosophical Society*, vol. 84, Cambridge Univ Press, 549–567.

A Height-Correlated Masking and Shadowing for Transmission

We demonstrate the result of Eq. (8), i.e. that the height-correlated masking-shadowing function with transmission is the Beta function [Pinel et al. 2005]. If ω_o is transmitted, then it is on the other side of the microsurface. The masking function is obtained by vertically flipping the configuration, i.e.

$$G_1^{\text{dist}}(\omega_o) = (1 - C^1(h))^{\Lambda(-\omega_o)}.$$

The height-correlated masking-shadowing function is

$$\begin{aligned} G_2^{\text{dist}}(\omega_i, \omega_o) &= \int_{-\infty}^{+\infty} G_1^{\text{dist}}(\omega_i, h) G_1^{\text{dist}}(-\omega_o, -h) P^1(h) dh \\ &= \int_{-\infty}^{+\infty} C^1(h)^{\Lambda(\omega_i)} (1 - C^1(h))^{\Lambda(-\omega_o)} P^1(h) dh. \end{aligned}$$

If we substitute $H = C^1(h)$ then $dH = P^1(h) dh$ and since $H = C^1(h) \in [0, 1]$ the integral becomes

$$\begin{aligned} G_2^{\text{dist}}(\omega_i, \omega_o) &= \int_0^1 H^{\Lambda(\omega_i)} (1 - H)^{\Lambda(-\omega_o)} dH \\ &= B(1 + \Lambda(\omega_i), 1 + \Lambda(-\omega_o)). \end{aligned}$$

The Beta function B is available in e.g. the C++11 math library.

B Projected Area

We demonstrate the result of Eq. (22). From Eq. (9) and (10) we obtain Eq. (21):

$$\int_{\Omega} \langle \omega_n, \omega_m \rangle D(\omega_m) d\omega_m = (1 + \Lambda(\omega_n)) \cos \theta_n.$$

Since the signed, projected area of the microfacet is the projected area of the geometric surface [Walter et al. 2007] we have

$$\int_{\Omega} (\omega_n \cdot \omega_m) D(\omega_m) d\omega_m = \cos \theta_n.$$

By splitting this integral into its positive and negative components using the clamped dot products:

$$\begin{aligned} &\int_{\Omega} (\omega_n \cdot \omega_m) D(\omega_m) d\omega_m \\ &= \int_{\Omega} \langle \omega_n, \omega_m \rangle D(\omega_m) d\omega_m - \int_{\Omega} \langle -\omega_n, \omega_m \rangle D(\omega_m) d\omega_m, \end{aligned}$$

we get

$$\begin{aligned} &\int_{\Omega} \langle -\omega_n, \omega_m \rangle D(\omega_m) d\omega_m \\ &= \int_{\Omega} \langle \omega_n, \omega_m \rangle D(\omega_m) d\omega_m - \int_{\Omega} (\omega_n \cdot \omega_m) D(\omega_m) d\omega_m \\ &= (1 + \Lambda(\omega_n)) \cos \theta_n - \cos \theta_n \\ &= \Lambda(\omega_n) \cos \theta_n. \end{aligned}$$

C Free-Path PDF

We demonstrate the result of Eq. (27). The PDF is the differential of the CDF:

$$P_{h_r, \omega_r}^1(h_{r+1}) = \frac{\partial C_{h_r, \omega_r}^1(h_{r+1})}{\partial h_{r+1}}.$$

There are 3 cases in the CDF from Eq. (27):

- The regions behind the ray ($h_{r+1} < h_r$ if the ray is going up or $h_{r+1} > h_r$ if the ray is going down). In these regions the PDF is 0.
- The region that can be intersected by the ray is associated with the main part of the CDF, where

$$\begin{aligned} \frac{\partial C_{h_r, \omega_r}^1(h_{r+1})}{\partial h_{r+1}} &= \frac{\partial (1 - G_1^{\text{dist}}(\omega_r, h_r, \tau))}{\partial h_{r+1}} \\ &= -\frac{\partial \left(\frac{C^1(h_r)}{C^1(h_r + \tau \cot \theta_r)} \right)^{\Lambda(\omega_r)}}{\partial h_{r+1}}. \end{aligned}$$

Since the next height is $h_{r+1} = h_r + \tau \cot \theta_r$ because $\cot \theta_r$ is the slope of the ray direction, we have

$$-\frac{\partial \left(\frac{C^1(h_r)}{C^1(h_{r+1})} \right)^{\Lambda(\omega_r)}}{\partial h_{r+1}} = \Lambda(\omega_r) P^1(h_{r+1}) \frac{C^1(h_r)^{\Lambda(\omega_r)}}{C^1(h_{r+1})^{1+\Lambda(\omega_r)}}.$$

A subtlety is that if $\theta_r > \frac{\pi}{2}$, the CDF parametrization is flipped and a minus sign must be introduced in the PDF. In this case, the value of $\Lambda(\omega_r)$ is negative. Hence, in Eq. (27) we use the absolute value $|\Lambda(\omega_r)|$ and the formula is correct in either case.

- Some of the rays might leave the microsurface without intersecting it and the CDF of Eq. (27) has a special case $C_{h_r, \omega_r}^1(h_{r+1}) = 1$ if $\tau = \infty$. This discrete event is represented in the PDF by a Dirac delta distribution $\delta_{\infty}(h_r)$ whose amplitude is the probability of leaving the microsurface without intersection $G_1^{\text{dist}}(\omega_r, h_r, \infty)$.

The PDF of Eq. (27) is always positive and integrates to 1.

D Height Sampling

We demonstrate the result of Eq. (30). Sampling heights implies inverting the CDF of Eq. (27) such that for a given random number

$$\mathcal{U} = C_{h_r, \omega_r}^1(h_{r+1}) = 1 - G_1^{\text{dist}}(\omega_r, h_r, \tau).$$

With Eq. (25), if $\mathcal{U} \geq 1 - G_1^{\text{dist}}(\omega_r, h_r, \infty)$ the equation has no solution and the ray leaves the surface ($h_{r+1} = \infty$). Otherwise, if $\mathcal{U} < 1 - G_1^{\text{dist}}(\omega_r, h_r, \infty)$, we need to find τ such that

$$1 - \mathcal{U} = \exp \left(- \int_0^{\tau} \sigma_t^{\text{Smith}}(\omega_r, h_r + \tau' \cot \theta_r) \left| \left| \frac{\partial d}{\partial \tau} \right| \right| d\tau' \right).$$

This is similar to sampling distances in classic volumetric rendering (see e.g. [Raab et al. 2008, Eq. (12)]). With Eq. (25) we develop:

$$\begin{aligned} 1 - \mathcal{U} &= \left(\frac{C^1(h_r)}{C^1(h_{r+1})} \right)^{\Lambda(\omega_r)} \\ \Rightarrow (1 - \mathcal{U})^{1/\Lambda(\omega_r)} &= \frac{C^1(h_r)}{C^1(h_{r+1})} \\ \Rightarrow h_{r+1} &= C^{-1} \left(\frac{C^1(h_r)}{(1 - \mathcal{U})^{1/\Lambda(\omega_r)}} \right). \end{aligned}$$